J Solid State Electrochem
https://doi.org/10.1007/s10008-017-3823-9

ORIGINAL PAPER

Electrochemical machining of tungsten carbide

N. Schubert[1] · M. Schneider[2] · A. Michaelis[1,2] · M. Manko[3] · M. M. Lohrengel[3]

Received: 6 July 2017 / Revised: 3 November 2017 / Accepted: 6 November 2017

Abstract Electrochemical machining (ECM) is characterized amongst other things, by extremely high current densities and a high dissolution rate of material. Due to the extreme current densities under ECM conditions, tungsten carbide forms adherent, supersaturated, viscous films of polytungstates close to the interface. This film is permanently dissolved by electrolyte flow and is reproduced at the electrode surface. The dissolution proceeds in an active state up to 30 A cm^{-2}. An additional layer is formed at higher current densities which means that there is a passive state and the presence of high-field oxide films with thicknesses around 10 nm. The complex interaction between current, field strength, and oxide thickness yields a constant resistance to the oxide film. The formation of an oxide film is also indicated by the onset of oxygen evolution which consumes about 20% of anodic charge. The interaction of ionic currents (oxide formation and dissolution) and electronic currents (oxygen evolution) is small due to completely different conduction mechanisms.

Keywords Anodic dissolution · Electrochemical machining (ECM) · Tungsten carbide

✉ M. Schneider
Michael.Schneider@ikts.fraunhofer.de

[1] Institute of Material Science, TU Dresden, Helmholtzstr.7, 01067 Dresden, Germany

[2] Fraunhofer IKTS Dresden, Winterbergstr. 28, 01277 Dresden, Germany

[3] Heinrich-Heine-Universität Düsseldorf, Universitätsstr. 1, 40225 Düsseldorf, Germany

Introduction

Electrochemical machining (ECM) is an unconventional technique used to shape steel and other conductive materials and to produce high quality products. The basic principle is that of a specific anodic dissolution at high current densities between 5 and 100 A cm^{-2} in highly conductive electrolytes [1–4]. A detailed knowledge of the process is essential in order to obtain an optimized, economically attractive technique, but the dissolution mechanism of ECM is not completely understood. Due to the transient and harsh conditions, the investigations of dissolution mechanism under ECM conditions are quite difficult.

Some attempts to investigate and describe the dissolution process of certain metals are discussed in the literature [5, 6]. One main subject investigated for several metals such as iron, nickel, or copper is the distinction between active and transpassive dissolution mechanism owing to the close relation to the surface topography, machining accuracy, and current efficiency.

The anodic dissolution of common base metals such as iron and nickel is strongly influenced by the electrolyte: electrolytes containing halides such as chloride or bromide support the active dissolution mechanism. Characteristics of active dissolution are as follows:

- Direct passage of atoms into electrolyte as hydrated or complexed species
- Formation of an etch pattern due to preferential dissolution of energetically favored planes, kinks, and grain boundaries
- Kinetics expressed by Tafel behavior in the low potential region without control of mass transport
- High current efficiency, no oxygen evolution.

Published online: 15 November 2017

However, with oxidative or less aggressive electrolytes such as nitrates and chlorates, metal surfaces can passivate. This behavior is common in most electrolytes for valve metals such Al, Nb, Ta, and Ti. Hence, transpassive dissolution must be discussed.

Characteristics of transpassive dissolution are as follows:

- Formation of a surface layer, usually an oxide film of some nm
- Oxygen evolution as side reaction
- Lower current efficiency compared to active dissolution
- Kinetics controlled by mass transport in the layer
- Uniform dissolution, independent of the microstructure, which is a typical result of high-field oxide films.

Oxygen evolution seems to be coupled with the presence of an oxide film which means the oxide acts similar to a catalyst. Hence, it can be used as an indicator of transpassive dissolution [7].

The properties mentioned above were found for common current densities < 1 A cm^{-2}. Under ECM conditions, which are current densities >> 1 A cm^{-2}, a separation of active and transpassive dissolution is also possible. Fe dissolves in chloride solutions around 0 V without oxygen evolution and forms Fe^{2+} as a product. In nitrate solutions, however, a mixture of Fe^{2+}, Fe^{3+}, and O_2 is produced at potentials around 3 V, which indicates the presence of an oxide film [8]. Moreover, ECM in nitrate solutions yields higher machining accuracy and some polishing effects which correspond to the uniform dissolution mentioned above.

On the other hand, significant differences were observed at current densities >> 1 A cm^{-2}. Fundamental changes in kinetics were found and the common models of interface and diffusion transport cannot be applied at larger current densities.

Main product of anodization of Fe in nitrate solutions is oxygen at lower current densities (almost 100%), but at current densities > 5 A cm^{-2}, the system switches into another state with Fe^{2+} and Fe^{3+} as main products and much less oxygen (around 10%) [9]. This is also true for other metals, and, accordingly, special surface conditions were assumed, e.g., supersaturated viscous films (Cu in H_3PO_4 [10]; Fe-Cr in H_3PO_4, H_2SO_4 [11]), oxide films (Ni in $NaNO_3$ [12]), or salt films (Ni in $NaNO_3$ [13]; Fe in $NaNO_3$ [14]; Ni, Fe in NaCl [15]; Fe, Ni in $NaNO_3$ or $NaClO_3$ [16]; Ni in NaCl [17]).

Detailed computer simulations predicted highly supersaturated product films and extreme concentrations of H^+ at the surface at some 10 A cm^{-2} [6, 18]. Fortunately, such supersaturated product films can be produced in bulk scale for nitrates of Cr, Fe, Mn, and Ni, and some of their properties such as viscosity or conductivity can be easily determined [4]. Accordingly, the model of supersaturated, viscous product films was favored which also explains the polishing effect. The limitation of mass transport of water through the product film reduces the activity of free water and explains the reduced oxygen evolution.

As already mentioned, ECM is a perfect technique for machining hard materials such as carbides or nitrides since the hardness of the work-piece has no influence on the process. This study focusses on the anodic dissolution behavior of tungsten carbide in alkaline electrolyte under ECM conditions. Polarization curves of tungsten carbide in sodium hydroxide electrolyte, in situ investigations of the development of the surface structure during the ECM-process, were carried out, as well as analytical investigations of reaction products such as oxygen. The dissolution mechanism and the structure of the interface are discussed, based on the experimental results of this work.

Material and methods

Materials

The materials used were commercially available tungsten with a purity of 99.95% (MaTeck GmbH) and non-commercial, binder-free tungsten carbide samples. These binder-free samples were produced in-house (IKTS) by the sintering of two different tungsten carbide powders of almost identical chemical composition but different particle sizes which then results in different grain sizes after the sintering process (Table 1).

The tungsten sample was mechanically ground with SiC-paper of different grades (P120, P180, P280) and polished with diamond suspensions of various grain sizes (15, 3, 1, 0.1 μm). The tungsten carbide samples were mechanically lapped. Due to the lack of binder material, the samples have pores as shown in the scanning electron microscope (SEM) images (Fig. 1).

Before the electrochemical experiments, the samples were rinsed with deionized water and degreased with ethanol. The electrolyte used was a 1 M NaOH solution prepared of sodium hydroxide pellets p.a. (Carl Roth) and deionized water.

Methods

Potentiodynamic experiments close to the equilibrium potential of the samples (working electrode (WE)) were carried out using a top-frame cell as shown schematically in

Table 1 Characterization of the used WC powder. The indices of *d* indicates the fraction of powder particles of represented sizes

Powder	d_{10} /μm	d_{50} /μm	d_{90} /μm	*C* %	*O* %
WC2000	15.9	42.6	121.9	6.15	0.01
WC600	4.2	10.1	20.9	6.09	0.03

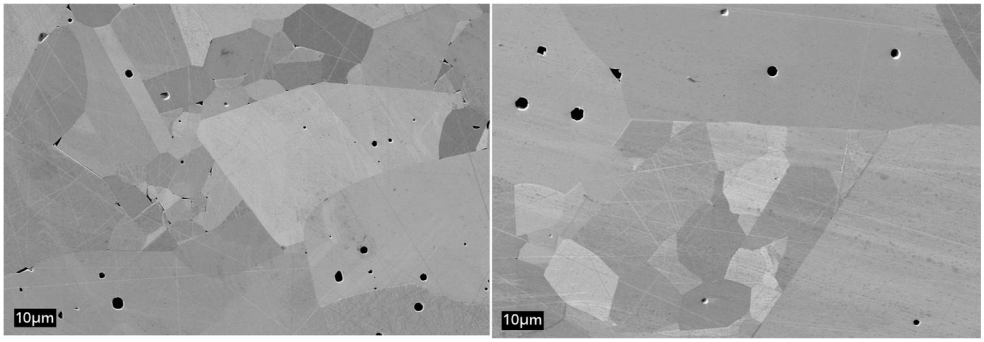

Fig. 1 SEM images of the tungsten carbide samples (magnitude × 1000), left WC600, right WC2000

Fig. 2. Platinum was used as a counter electrode (CE), and a saturated calomel reference electrode (RE) was used to perform experiments in a 3-electrode set-up. All given potentials were calculated against the standard hydrogen electrode (SHE). The top-frame cell was coupled with a computer controlled potentiostat AUTOLAB PGSTAT 30 (Deutsche Metrohm GmbH).

Anodic sweep experiments with this set-up were carried out in a potential range of − 1.2 to 0 V vs SHE with a sweep rate of 1 mV s^{-1}.

The potentiodynamic experiments under ECM conditions were carried out in a so-called Theta-cell, a microelectrochemical equipment first introduced by Moehring and Lohrengel [6, 19]. The Theta-cell was coupled with a computer controlled potentiostate IMP88-200 V (IPS Ing.büro P. Schrems, Germany). All potentials were measured versus a 3 M Ag/AgCl reference electrode and calculated against the standard hydrogen electrode. A gold wire was used as counter electrode. To get information about current efficiency, the Theta-cell was coupled with online-analysis of oxygen [20]. Therefore, a fluorescence active complex (dichlorotris(1,10-phenantroline)ruthenium(II)hydrate) was added to the electrolyte. The fluorescence is quenched due to the dissolved oxygen. This effect can be quantified and was measured in the outlet of the Theta-cell. A modification of the set-up allowed some excess pressure to keep all oxygen dissolved.

To investigate the surface conditions of the anode at different current density also, galvanostatic experiments were carried out in a specifically designed flow channel cell [7]. A scheme of the cell is shown in Fig. 3. Anode and cathode are arranged directly opposite each other at a distance of 350 µm. Gold is used as a cathode material. A very small hole within the cathode, where a glass lens is located, enables the observation of the anode surface directly by a light microscope positioned above the cathode. Therefore, phenomena such as gas evolution and the development of the microstructure at the anode surface occurring during anodic polarization can be observed in situ. A 3 M Ag/AgCl reference electrode was implemented in the lid of the cell to measure the potential of the anode during anodic polarization. Galvanostatic experiments were carried out at 5, 10, 14, 20, 30, and 40 A cm^{-2} for 5 and 10 s, respectively. In this work, we focus on in situ observation at 5 A cm^{-2} for detailed information about visible gas evolution and development of the microstructure at the lower potential range. Therefore, electron backscatter diffraction (EBSD) measurements were carried out in a scanning electron microscope Nvision 40 with a Schottky-emitter (Carl Zeiss SMT AG). Preliminary to the electrochemical

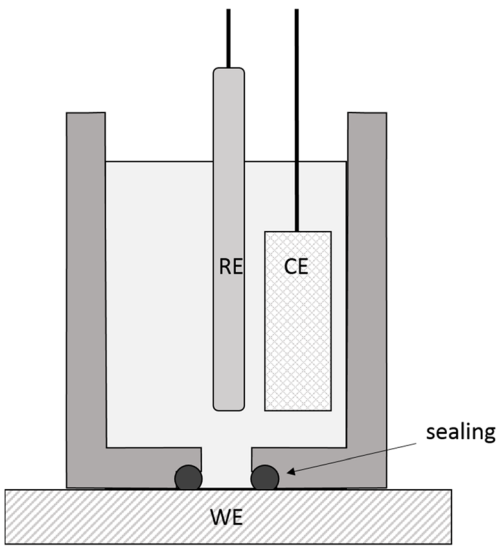

Fig. 2 Experimental set-up with a top-frame cell

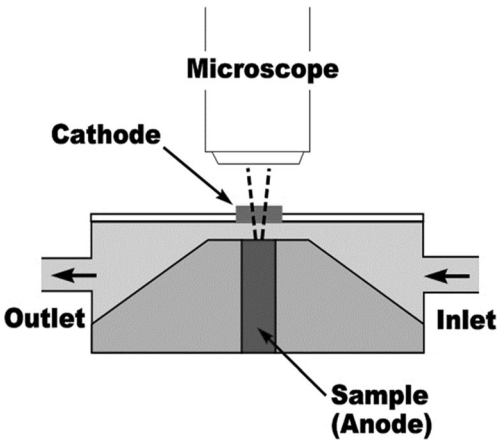

Fig. 3 Scheme of the channel flow cell with coupled microscope

treatment in the flow channel cell, the samples were rinsed with water and ethanol. Current controlled pulse experiments were carried out at 5 A cm^{-2} with a pulse on-time of 1 s and a pulse off-time of 1 s. Two pulses were applied.

Tungsten and tungsten carbide

Anodic behavior of tungsten

Tungsten is covered by thin stable oxide layers under atmospheric conditions, as well as in acidic solutions and neutral solutions. The oxide is reported to be an amorphous WO_3 [21].

Hence, the oxide is formed in acidic or neutral solutions according to

$$W + 3\ H_2O \rightarrow WO_3 + 6\ H^+ + 6\ e^- \quad (1)$$

Corrosion in acidic media leads to "tungstenyl" cations:

$$W + 2\ H_2O \rightarrow WO_2^{2+} + 4\ H^+ + 6\ e^- \quad (2)$$

Tungstates are formed in alkaline solutions, formally

$$W + 4\ H_2O \rightarrow WO_4^{2-} + 8\ H^+ + 6\ e^- \quad (3)$$

and can polymerize by condensation reactions to polytungstates, e.g.,

$$W + 4\ H_2O \rightarrow WO_4^{2-} + 8\ H^+ + 6\ e^- \quad (4)$$

The anodic oxide film growth follows a high-field mechanism [22, 23] at field strengths > 6 MV cm^{-1} [24–26]. The transport number of cations is 0.35 at 100 μA cm^{-2} and increases slightly with current density [27].

Some of these data in the literature are inconsistent or not applicable to our conditions. Therefore, we recorded cyclovoltammograms in less corrosive media (pH < 8). We found in aqueous $NaNO_3$, NaCl, and H_2SO_4 small activation peaks around 1 V followed by a constant plateau current $i_{Plateau} \approx 190$ μA cm^{-2} at a sweep rate $dU/dt = 100$ mV s^{-1} [28]. We can calculate a formation factor k from $i_{Plateau}$ according to Faraday's law

$$k = \frac{M \cdot i_{Plateau}}{\rho \cdot z \cdot F \cdot dU/dt} \quad (5)$$

and obtain with the molecular mass ($M = 231.85$ g Mol^{-1}), the density ($\rho = 7.16$ g cm^{-3}), and the number of electrons per Mol ($z = 6$)

$$k = 1.063\ \text{nm V}^{-1}$$

The inverse formation factor $1/k$ is the oxide formation field strength for these conditions, $E = 9.41$ MV cm^{-1} [28].

The currents in the cathodic sweep are close to zero, altogether the common behavior of valve metals and high-field growth.

Anodic behavior of tungsten carbide

The behavior is very similar to W. The anodic dissolution of WC in alkaline solutions will follow

$$WC + 7\ H_2O \rightarrow WO_4^{2-} + CO_3^{2-} + 14\ H^+ + 10\ e^- \quad (6)$$

Prerequisite, however, are conditions at the interface which are equal to the bulk electrolyte (here 1 M NaOH).

Systems under ECM conditions with current densities of 10 or 100 A cm^{-2}, however, are far from an electrochemical equilibrium and must not correspond to thermodynamic data. These extreme current densities and massive convection allow a high dissolution rate of the material which is so high that common models of diffusion, electrolytic conductivity, and aqueous electrochemistry cannot be applied anymore.

Despite the high electrolyte velocity, there is a hydrodynamic boundary layer, which allows the formation of a thin, highly supersaturated layer of reaction products at current densities >> 1 A cm^{-2}. Large numbers of protons are released (Eqs. 1–5), leading to a huge pH shift to lower values. To state a pH value, however, is critical as it is defined as a scale of acidity or basicity of diluted aqueous solutions, which is not applicable to these supersaturated layers. "Buffering" of the metal surface by 1 M NaOH will work up to around the current densities < 1 A cm^{-2} according to common diffusion models, but not under ECM conditions.

Altogether, we expect a layer of viscous supersaturated tungsten ions with a thickness of around 1 μm or less, which corresponds roughly to other ECM systems [9] and to hydrodynamic data. The composition of the tungsten species in the layer is unknown, WO_2^{2+} can be discussed. The concentration of water will be extremely low due to supersaturation; less than 10 molecules per ion, as we learned from other systems [6]. Hence, one can assume that the rate determining step is diffusion of water to the electrode surface. The supersaturated layer is continuously formed at the interface and dissolved in the electrolyte as tungstates.

A quantitative product analysis of TiC and TiN [29] showed a transition to products which require less water for formation with increasing current density. Therefore, in our case, a formation of CO_2 may be valid for low current densities only (Eq. 6). With increasing current density, a transition to CO and or even to C must be expected:

$$WC + 5\ H_2O \rightarrow WO_4^{2-} + CO + 10\ H^+ + 8\ e^- \quad (7)$$

or

$$WC + 4\ H_2O \rightarrow WO_4^{2-} + C + 8\ H^+ + 6\ e^- \quad (8)$$

Results and discussion

Voltammograms of W and WC

Figure 4 shows linear sweep voltammograms of W and WC in an unstirred 1 M NaOH electrolyte with pH 14. The transition potentials anodic/cathodic are − 0.46 V vs SHE for W and − 0.37 V vs SHE for WC, respectively, and are similar to open circuit potentials. These potentials are composed of different processes such as metal dissolution, oxygen reduction, and hydrogen evolution and, thus, are mixed potentials.

The Tafel slope of dissolution of W is 80 mV decade^{-1} and for WC 110 mV decade^{-1}. Therefore, the authors assume active dissolution of tungsten carbide in the lower potential region. Furthermore the semi-logarithmic plot of WC is very similar to pure W. The oxidation of W to WO_4^{2-} (Eq. 3) is identified as the dominating process in anodic dissolution of WC.

Figure 5 shows the linear sweep voltammograms of tungsten carbide in a microcapillary flow cell under ECM conditions. There are two linear regions, one up to 25 A cm^{-2} and a second one from 35 A cm^{-2}. Linearity in potential-current-plots means ohmic behavior which is rare in electrochemistry and normally limited to ionic conductivity in electrolytes. Accordingly, the first slope with 0.4 Ω cm^{-2} corresponds to the electrolyte resistance $R_{\text{electrolyte}}$ between sample and counter electrode. The second slope of 0.6 Ω cm^2 means an additional ohmic resistance ($R_{>30\text{V}} = 0.2\ \Omega\ \text{cm}^{-2}$) in series and therefore, a newly formed layer.

This means that we get an equivalent circuit (Fig. 6) which explains the data of Fig. 5: the impedance of the metal interface (R_{IF} with a thickness around some nm), the resistance $R_{>30\text{V}}$, which is present only at current densities > 35 A cm^{-2}, and the electrolyte resistance $R_{\text{electrolyte}}$ which

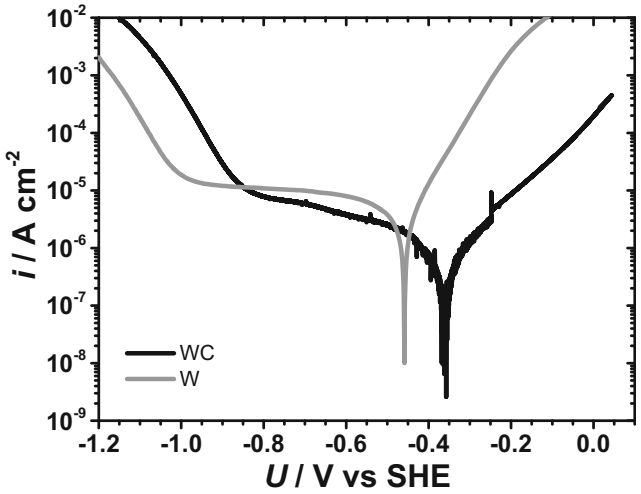

Fig. 4 Semi-logarithmic plot of the linear sweep voltammograms of W (gray) and WC (black) in 1 M NaOH, $U = -1.2$ to 0 V vs. SHE, dU/dt = 1 mV s^{-1}

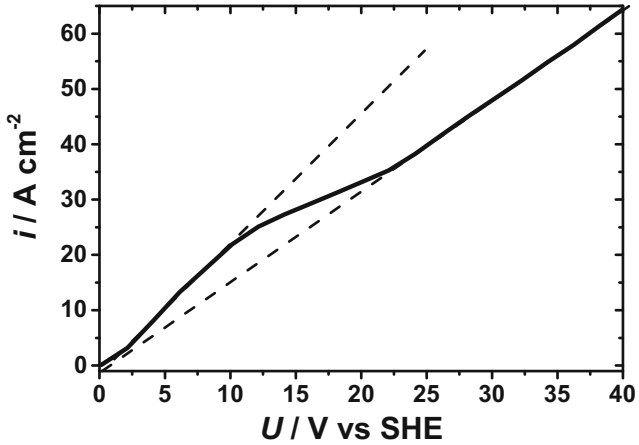

Fig. 5 Linear sweep voltammograms of WC in 1 M NaOH obtained in a microcapillary cell, $U = 0$–40 V vs SHE, $dU/dt = 2$ V s^{-1}

includes the supersaturated film with an estimated thickness around 1 μm. This current density of transition in Fig. 5 depends, however, on experimental conditions, especially the flow rate and cell geometry.

The metal/electrolyte interface kinetics and, thus, R_{IF} are often described by a Butler-Volmer-mechanism, which means an exponential dependence of current on potential with typical values around 100 mV decade^{-1} of current. Hence, we expect a potential shift of less than 200 mV maximum for current densities changing less than 2 decades which remains almost invisible.

The supersaturated polytungstate layer will be formed at current densities larger than 5 A cm^{-2}. It will be less conductive than the electrolyte, but, due to its small thickness and almost constant thickness, it cannot be distinguished from $R_{\text{electrolyte}}$.

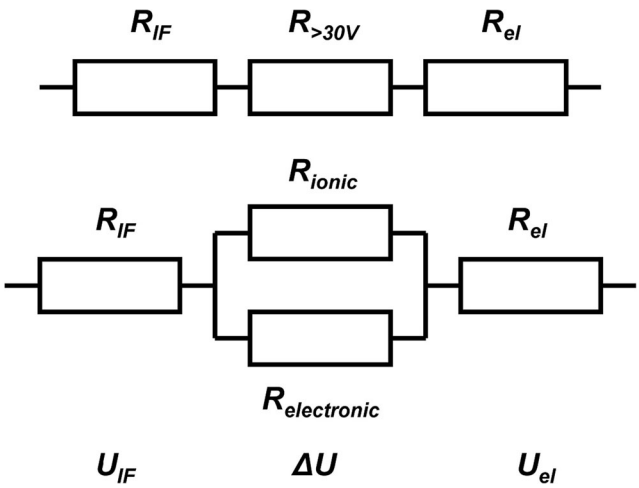

Fig. 6 Equivalent circuits for linear sweep voltammograms of WC in 1 M NaOH for current densities > 35 A cm^{-2} as from experiments (top), interpreted as oxide film (center), and corresponding potential drops (bottom). The indices IF and el mean interface and electrolyte, respectively

Surprising is the ohmic behavior of $R_{>30V}$, which means, the "> 30 V-structure" seems to be independent of the dissolution rate and its thickness does not change with the current. As will be discussed in the next section this is not true.

Current efficiency

Figure 7 shows the rate of oxygen evolution (or oxygen efficiency) according to

$$2\,H_2O \rightarrow O_2 + 4\,H^+ + 4\,e^- \quad (9)$$

as a function of applied current density. Up to 30 A cm^{-2} no oxygen was detected in the electrolyte. This corresponds to an active dissolution below this current density.

The oxygen evolution rises between 30 and 50 A cm^{-2}, finally consuming up to 20% of the applied anodic charge. This corresponds to significant changes of slope in Fig. 6. Obviously, the active state has changed into a passive one, as oxygen evolution is always coupled to the presence of oxide films, which has been already mentioned above. This means, $R_{>30V}$ represents an anodic oxide film.

Surprising is the ohmic behavior of this oxide film. One could calculate a "specific resistance" provided the thickness of oxide is known and constant. This is, however, in contrast to the assumption of high-field oxide films on W. For these systems, the current density of oxide growth i_{ox} depends exponentially on the field strength E within the oxide, and linearity is not expected.

The experimental current includes three components: the ionic currents of oxide growth i_{ox} and oxide dissolution i_{diss} and the electronic current of oxygen evolution i_{O2}. The ionic currents must follow the high-field equation

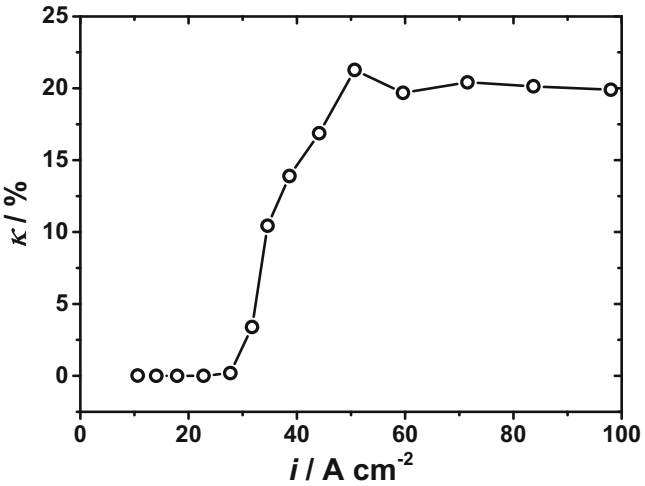

Fig. 7 Efficiency of oxygen evolution during ECM of WC in 1 M NaOH at current densities up to 100 A cm^{-2}

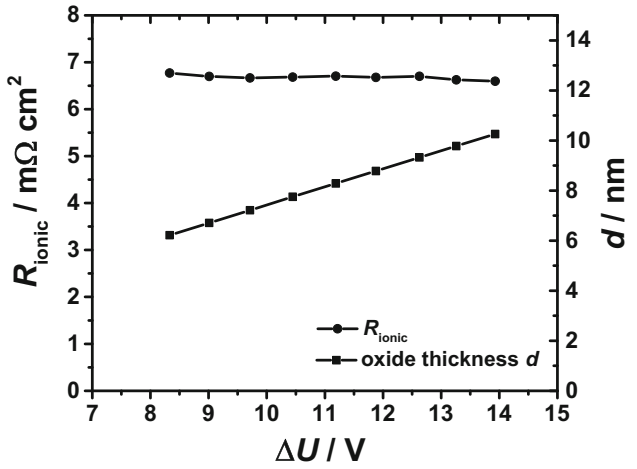

Fig. 8 Potential dependent oxide thicknesses d, calculated from Eq. 12, for current densities > 30 A cm^{-2}

$$i_{ox} + i_{diss} = i_{ionic} = i_0 \cdot \exp(\beta E) = i_0 \cdot \exp\left(\frac{\beta}{k}\right) = i_0 \cdot \exp\left(\beta \frac{\Delta U}{d}\right) \quad (10)$$

with oxide specific constants β and i_0. The field strength E can be substituted by the inverse formation factor $1/k$ [30] or by the potential drop across the oxide film ΔU and the oxide thickness d. We can try to work with high-field data from pure W (section 3.1). The problem is to get reliable data for β and i_0. Most data for β in the literature are around 30 nm V^{-1} [30]. Using this value, i_0 can be calculated from $i_{Plateau}$ and k (Eq. 10) and we get $i_0 = 1.05 \cdot 10^{-16}$ A cm^{-2}.

Equation 10 was used to determine oxide thicknesses at current densities > 30 A cm^{-2}. The potential drop across the oxide ΔU is calculated from the experimental potential U, from the interface potential U_{IF}, extrapolated for $i = 0$ in Fig. 5 ($U_{IF} = 0.626$ V) and from the potential drop in the

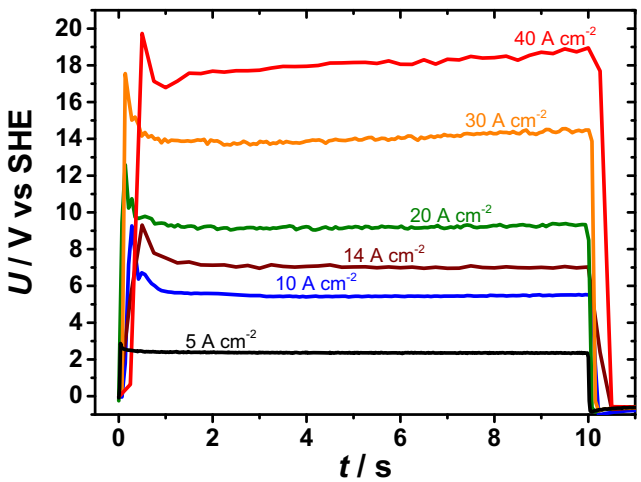

Fig. 9 Transients of galvanostatic experiments at 5, 10, 14, 20, 30, and 40 A cm^{-2} on WC in 1 M NaOH in a channel flow cell

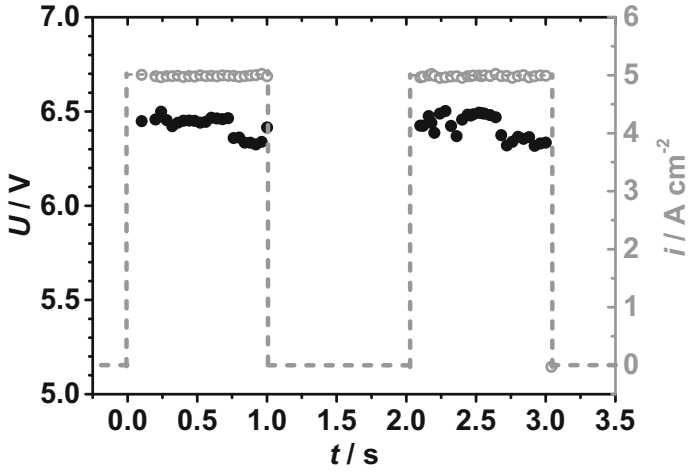

a) Voltage and current density vs. time plot.

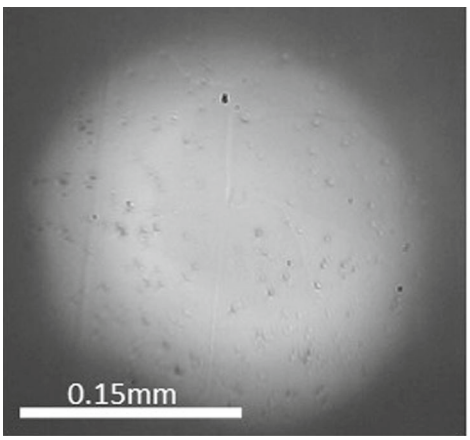

b) Microscopic view on the WC surface at initial state (t = 0 s).

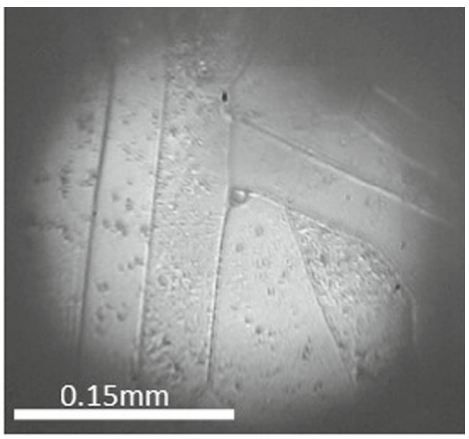

c) Microscopic view on the WC surface after the first pulse (t = 1.226 s).

Fig. 10 Galvanostatic double pulse experiment on WC in 1 M NaOH at $i = 5$ A cm^{-2} (**a**) with simultaneous observation of the anode surface (**b**, **c**)

electrolyte:

$$\Delta U = U - U_{IF} - R_{el} \cdot i \tag{11}$$

R_{el} has already been determined in "Voltammograms of W and WC" section. Then, oxide thicknesses d are given by

$$d = \frac{\beta(\Delta U)}{\ln\left(\frac{i}{i_0}\right)} \tag{12}$$

Figure 8 shows these data. The oxide thickness depends linearly on the potential.

The next step is to determine the resistance of the oxide film, formerly called $R_{>30V}$. As we expect a non-linear behavior, which means a potential dependent resistance, we must handle $R_{ionic} = \partial U / \partial i_{ionic}$ as a differential resistance. I_{ionic} is calculated from the experimental current density i according to

$$i_{ionic} = i - i_{electronic} = 0.8 \cdot i \tag{13}$$

as ≈ 20% of the total charge are consumed for oxygen evolution. The interaction between i_{ionic} and $i_{electronic}$ is small due to the completely different mechanism (quantum mechanical resonance tunneling of electrons; see e.g., [31, 32]). Based on Eq. 10, R_{ionic} can be calculated as follows:

$$R_{ionic} = \frac{\partial U}{\partial i_{ionic}} = \frac{d}{\beta \cdot i_0 \cdot \exp\left(\beta \frac{\Delta U}{d}\right)} = \frac{d}{\beta \cdot i_{ionic}} \tag{14}$$

This means, R_{ionic} is constant since both, d and i_{ionic}, depend linearly on the potential (Figs. 5 and 8). We can even get numeric values from Eq. 14, $R_{ionic} = 0.007\ \Omega\ \text{cm}^2$. This value, however, is about one decade smaller than 0.2 Ω cm^2, taken from Fig. 6. There may be different reasons for this:

- The high-field data used here were taken from current densities more than 5 decades smaller than in ECM experiments.
- The high-field data were taken from experiments with pure tungsten. The carbon in WC will cause changes.

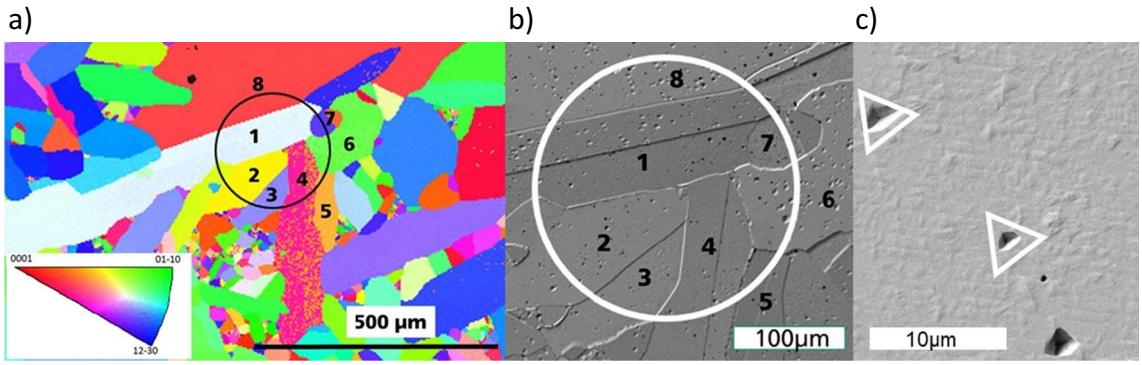

Fig. 11 EBSD pattern before and SEM images after the ECM of WC at 5 A cm^{-2} shown in Fig. 10. **a** EBSD pseudo color plot. (The black circle and the Arabian numerals indicate the microstructure of the sample section which is also visible in Fig. 10.) The inverse pole figure indicates serves for identification of the grain orientation (red: basal plane, green: pyramidal plane). **b** SEM image of WC after the ECM experiment. (The black circle and the Arabian numerals indicate the microstructure of the sample section which is also visible in Fig. 10.). **c** SEM image of a section of grain 2 after the ECM experiment

Nevertheless, it was demonstrated that our ECM data can be explained by an active/passive transition around 35 A cm^{-2} and a high-field oxide growth.

Galvanostatic transients and surface structure

Galvanostatic experiments were carried out in a flow channel cell. Figure 9 shows the transients of the potential at different applied current densities. After a short overshoot in the beginning, the potential becomes constant finally at current densities below 20 A cm^{-2}. At 30 and 40 A cm^{-2}, the potential slightly increases indicating an ascending resistivity, due to formation of an oxide layer with oxygen evolution. Overall, the graph is in agreement with Fig. 5. Therefore, the authors assume comparable and reproducible conditions for tungsten carbide dissolution in various experimental set-ups.

The channel flow cell used for galvanostatic experiments (Fig. 3) provides microscopically in situ observation of the anode surface. Therefore a current controlled pulse experiment was carried out on a tungsten carbide sample characterized by EBSD. Potential and current density time plots are shown in Fig. 10a.

Figure 10b, c shows images of the sample surface at different states of the experiment. The initial state is presented in Fig. 10b. The microstructure was slightly visible including a number of pores or defects. A clearly etched microstructure appeared in the pulse pause (Fig. 10c). Some of the grains were brighter and additional pores or defects became visible. There was no significant change of the microscopically observable section of the surface during the second pulse with respect to the etched state in the pulse pause. During the complete pulse experiment, WC dissolved without any visible gas formation, as current densities were $<<30$ A cm^{-2}.

Electron backscatter diffraction and scanning electron microscope

The development of the surface structure observed in the pulse experiment shown in Fig. 10 raises the question of whether the microstructure influences the dissolution of tungsten carbide at high current densities. Figure 11a shows the EBSD pattern of the WC sample before machining at 5 A cm^{-2}. The microscopically observed section of the sample, which is shown in Fig. 10, is marked by the black circle. Grains with different orientation are marked with different numbers. After machining, the sample surface was examined by SEM (Fig. 11b, c).

The microstructure at the sample surface became apparent as etch pattern and the individual grains are clearly visible. This is in agreement with the light microscopic observation. The material removal of individual grains is different and obviously depends on the crystallographic orientation. {0001}-oriented grains (basal plane parallel to the surface) or vicinal orientation and also {01–10}-oriented grains (pyramidal planes} are less attacked, whereas {12–30}-oriented grains are attacked preferentially, which results in a distinct surface topography (see Fig. 11b). The basal plane in hdp-materials is the closed packed plane, and the results fit to our own earlier study on copper [33] as well as the theoretical deliberations of Landolt [34]. This is distinct evidence of an active dissolution mechanism of tungsten carbide in sodium hydroxide solution at current densities < 30 A/cm^2. While Fig. 11b is an overview SEM image of the machined surface and especially the light-microscopically visible section during ECM, Fig. 11c zooms in on a less attacked grain. The visible pits are not pores but perforation points of dislocation. These perforation points are preferentially attacked due to the therein stored energy which decreases the working function. The shape of these etch figures strictly depends on the grain orientation, e.g., etch pits are

equilateral triangle pattern on {0001} basal planes in hdp-crystals [35]. The deviation from this ideal triangle characterized the deviation of the plane from the basal plane.

Conclusions

The extreme current densities form a WC electrode interface which cannot be described by common models of diffusion based on diluted systems. Close to the interface, an adherent, supersaturated, viscous film of polytungstates is formed which is continuously dissolved and reproduced. The cell potential is mainly determined by the electrolyte resistance between sample and counter electrode ($R_{electrolyte} = 0.4\ \Omega\,cm^2$ in our set-up). The dissolution proceeds in active state up to 30 A cm^{-2}. At current densities > 30 A cm^{-2}, an additional layer with a pseudo-ohmic resistance of 0.2 $\Omega\,cm^2$ is formed. This is not a current independent layer with a given "specific resistance" but reflects a passive state and high-field oxide films with thicknesses around 10 nm. The complex interaction between current, field strength, and oxide thickness yields a constant resistance of the oxide film.

The formation of an oxide film and, therefore, the active/passive transition is also indicated by the onset of oxygen evolution which cannot take place on bare metal surfaces but requires oxide films [8]. The current density of active/passive transition is not a natural constant but varies with experimental parameters such as electrolyte flow rate and cell geometry. Oxygen evolution consumes about 20% of the anodic charge. However, the interaction of ionic and electronic currents is small due to completely different conduction mechanisms.

Acknowledgements The authors gratefully thank the German Research Foundation (DFG) for their financial support (LO 319/16-2, MI 509/16-2, and SCHN 745/11-2).

References

1. Bannard J (1977) Electrochemical machining. J Appl Electrochem 7(1):1–29. https://doi.org/10.1007/BF00615526
2. Datta M (1993) Anodic dissolution of metals at high rates. IBM J Res Dev 37(2):207–226. https://doi.org/10.1147/rd.372.0207
3. McGeough J (1974) Priciples of electrochemical machining. Chapman and Hall, London
4. Schneider M, Lohrengel MM (2017) Electrochemical machining. In: Breitkopf C, Swider-Lyons K (eds) Springer-Handbook of Electrochemical Energy. Springer, Dordrecht, pp 941–971
5. Landolt D (1972) Flow channel cell apparatus for high rate electrolysis studies. Rev Sci Instrum 43(4):592–595. https://doi.org/10.1063/1.1685699
6. Lohrengel MM, Rosenkranz C, Klüppel I, Moehring A, Bettermann H, van Bossche BD, Deconinck J (2004) Electrochim Acta 49(17-18):2863–2870. https://doi.org/10.1016/j.electacta.2004.01.068
7. Schneider M, Schroth S, Schubert N, Michaelis A (2012) In-situ investigation of the surface-topography during anodic dissolution of copper under near-ECM conditions. Mater Corros 63(2):96–104. https://doi.org/10.1002/maco.201005716
8. Bockris JOM, Khan SUM (1993) Surface electrochemistry—a molecular level approach. Plenum Press, New York. https://doi.org/10.1007/978-1-4615-3040-4
9. Rosenkranz C, Lohrengel MM, Schultze JW (2005) The surface structure during pulsed ECM of iron in NaNO3. Electrochim Acta 50(10):2009–2016. https://doi.org/10.1016/j.electacta.2004.09.010
10. Glarum SH, Marshall JH (1985) J Electrochem Soc 132:2872–2885
11. Matlosz M, Magaino S, Landolt D (1994) J Electrochem Soc 141: 410–418
12. Datta M, Mathieu HJ, Landolt D (1979) Anodic film studies on nickel under high rate transpassive dissolution conditions. Electrochim Acta 24(8):843–850. https://doi.org/10.1016/0013-4686(79)87007-3
13. Datta M, Landolt D (1975) J Electrochem Soc 122:1466–1472
14. Datta M, Mathieu HJ, Landolt D (1984) J Electrochem Soc 131: 2484–2489
15. Datta M, Landolt D (1980) On the role of mass transport in high rate dissolution of iron and nickel in ECM electrolytes—I. Chloride solutions. Electrochim Acta 25(10):1255–1262. https://doi.org/10.1016/0013-4686(80)87130-1
16. Datta M, Landolt D (1980) On the role of mass transport in high rate dissolution of iron and nickel in ECM electrolytes—II. Chlorate and nitrate solutions. Electrochim Acta 25(10):1263–1271. https://doi.org/10.1016/0013-4686(80)87131-3
17. Datta M, Landolt D (1981) Electrochemical machining under pulsed current conditions. Electrochim Acta 26(7):899–907. https://doi.org/10.1016/0013-4686(81)85053-0
18. Lohrengel MM (2005) Pulsed electrochemical machining of iron in nano3: fundamentals and new aspects. Mater Manuf Process 20(1): 1–9. https://doi.org/10.1081/AMP-200041591
19. Moehring A (2004) Entwicklung einer elektrochemischen Durchflusszelle zur Untersuchung des Elektrochemischen Senkens (ECM, Electrochemical Machining). Dissertaion thesis, Heinrich-Heine-Universität, Düsseldorf
20. Rataj K, Hammer C, Walther B, Lohrengel MM (2013) Quantified oxygen evolution at microelectrodes. Electrochim Acta 90:12–16. https://doi.org/10.1016/j.electacta.2012.12.009
21. Aladjem A, Brandon DG, Yahalom J (1970) Electron-beam crystallization of anodic oxide films. Electrochim Acta 15(5):663–671. https://doi.org/10.1016/0013-4686(70)90029-0
22. Ammar IA, Salim R (1971) Anodic behaviour of tungsten—I. Oxidation kinetics in acid media. Corros Sci 11(8):591–609. https://doi.org/10.1016/S0010-938X(71)80056-2
23. Ammar IA, Salim R (1972) Anodic polarization of tungsten in neutral and alkaline solutions under conditions of anode film growth. Werkst Korros 23(3):161–167. https://doi.org/10.1002/maco.19720230302
24. Di Quarto F, Di Paola A, Sunseri C (1980) J Electrochem Soc 127: 1016–1021
25. Vermilyea DA (1963) Journal of The Electrochem Society 110:345
26. Arora MR, Kelly R (1977) J Electrochem Soc 124:1493–1499
27. Khalil N, Leach JS (1986) The anodic oxidation of valve metals—I. Determination of ionic transport numbers by α-spectrometry. Electrochim Acta 31(10):1279–1285. https://doi.org/10.1016/0013-4686(86)80148-7
28. Rataj KP (2013) Elektrochemische Charakterisierung technisch relevanter anodischer Oxidschichten bei niedrigen und höchsten Stromdichten. dissertation thesis, Heinrich-Heine-Universität Düsseldorf
29. Walther B, Schilm J, Michaelis A, Lohrengel MM (2007) Electrochemical dissolution of hard metal alloys. Electrochim

Acta 52(27):7732–7737. https://doi.org/10.1016/j.electacta.2006.12.038
30. Lohrengel MM (1993) Mat Sci Eng R11:243–294
31. Schultze JW, Vetter KJ (1973) The influence of the tunnel probability on the anodic oxygen evolution and other redox reactions at oxide covered platinum electrodes. Electrochim Acta 18(11):889–896. https://doi.org/10.1016/0013-4686(73)85043-1
32. Schultze JW (1970) Potentiostatische Messungen zur Sauerstoffentwicklung und Oxidschichtbildung an Platinelektroden. Z Phys Chem 73(1_3):29–47. https://doi.org/10.1524/zpch.1970.73.1_3.029
33. Schneider M, Schroth S, Richter S, Hohn S, Schubert N, Michaelis A (2011) In-situ investigation of the interplay between microstructure and anodic copper dissolution under near-ECM conditions—Part 1: the active state. Electrochim Acta 56(22):7628–7636. https://doi.org/10.1016/j.electacta.2011.06.075
34. Landolt D (2007) Corrosion and surface chemistry of metals. EPFL Press Lausanne: 59–61 and 89–91
35. Chung-Cherng L, Pouyan S (1993) Role of screw axes in dissolution of willemite. Geochim Cosmochim Acta 57(8):1649–1655. https://doi.org/10.1016/0016-7037(93)90104-5